Check for updates

Antitumor effects of a Sb-rich polyoxometalate on non-small-cell lung cancer by inducing ferroptosis and apoptosis†

Jie-Wei Lin,‡[a] Yang Zhou,‡[bc] Hui-Ping Xiao,‡[b] Lei-Lei Wu, [ID][d] Peng-Cheng Li,[e] Ming-Dong Huang,[bc] Dong Xie,*[a] Peng Xu,*[c] Xin-Xiong Li [ID] *[b] and Zhi-Xin Li*[a]

Polyoxometalates (POMs) are a class of anionic metal–oxygen clusters with versatile biological activities. Over the past decade, an increasing number of POMs, especially Sb-rich POMs, have been proven to exert antitumor activity. However, the antitumor effects and mechanisms of POMs in the treatment of non-small cell lung cancer (NSCLC) remain largely unexplored. This study employed a Sb-rich $\{Sb_{21}Tb_7W_{56}\}$ POM (POM-1) for NSCLC therapy and investigated its mechanism of action. Our results demonstrated that POM-1 exhibited cytotoxicity against H1299 and A549 cells with IC_{50} values of 3.245 μM and 3.591 μM, respectively. The migration and invasion were also inhibited by 28.05% and 76.18% in H1299 cells, as well as 36.88% and 36.98% in A549 cells at a concentration of 5 μM. In a tumor xenograft mouse model, POM-1 suppressed tumor growth by 76.92% and 84.62% at doses of 25 and 50 mg kg^{-1}, respectively. Transcriptomic analysis indicated the alteration of ferroptosis and apoptosis signaling pathways in POM-treated NSCLC cells. Subsequent experimentation confirmed the induction of ferroptosis, evidenced by 5.6-fold elevated lipid peroxide levels with treatment of 5 μM POM-1, alongside increased expression of ferroptosis-associated proteins. Additionally, the apoptosis induced by POM-1 was also validated by the 19.67% and 30.1% increase in apoptotic cells in H1299 and A549 cells treated with 5 μM POM-1, respectively, as well as the upregulated activation of caspase-3. In summary, this study reveals, for the first time, ferroptosis as the antitumor mechanism of Sb-rich POM, and that synergism with ferroptosis and apoptosis is a highly potent antitumor strategy for POM-based antitumor therapy.

[a]Department of Thoracic Surgery, Shanghai Pulmonary Hospital, School of Medicine, Tongji University, Shanghai 200433, China. E-mail: saklizhixin@163.com; kongduxd@163.com

[b]College of Chemistry, Fuzhou University, Fuzhou, Fujian 350108, China. E-mail: lxx@fzu.edu.cn

[c]College of Biological Science and Engineering, Fuzhou University, Fuzhou, Fujian 350108, China. E-mail: pengxu@fzu.edu.cn

[d]Department of Thoracic Surgery, Zhejiang Cancer Hospital, Hangzhou Institute of Medicine (HIM), Chinese Academy of Sciences, Hangzhou, Zhejiang 310005, China

[e]Shanghai Tumor Hospital, Fudan University, Shanghai 200032, China

† Electronic supplementary information (ESI) available: Synthetic details, structural figures, and spectrum data. See DOI: https://doi.org/10.1039/d4sc03856h

‡ These authors are contributed equally to this work.

1 Introduction

Lung cancer ranks among the most prevalent diagnosed cancers and stands as the leading cause of cancer-related death globally.[1] As the predominant histological subtype of lung cancer, non-small-cell lung cancer (NSCLC) encompasses approximately 85% of all lung cancer cases and represents a significant burden with a substantial fatality rate.[2] Despite notable progress in the diagnosis and therapeutics, NSCLC patients are still suffering from the exhaustion of therapeutic modalities, resulting in a low 5 years survival rate for those with advanced-stage NSCLC.[3] Although utilized as the primary management for NSCLC, chemotherapy normally exhibits insufficient therapeutic efficacy and is accompanied by severe adverse effects, including myelosuppression.[4] Therefore, the development of alternative therapeutic strategies with promoted antitumor effects and lower adverse effects is still highly demanded.

Polyoxometalates (POMs) are an emerging class of poly-nuclear metal–oxygen anion clusters featuring early transition metal ions (*e.g.*, V, Nb, Ta, Mo, and W) in their highest oxidation state with enormous structural and compositional diversity.[5–7] POMs have been developed for nearly two centuries and have a wide range of potential applications in fields ranging from material science to nanotechnology, due to their unique properties such as redox activity, thermal stability, and interesting catalytic, magnetic, photo- and electrochemical properties.[8–11] Additionally, POMs possess several adjustable features at the molecular level, such as size, shape, polarity, surface charge distribution, redox potential, and acidity, which make this

group of inorganic compounds suitable for potential medicinal uses.[12] To date, POMs have been demonstrated to possess antibacterial, antiviral, and antitumor activities, but the understanding of POMs' medicinal properties is still in their infancy and there is still a huge space for long-term exploration.[13–15]

In recent decades, increasing evidence has highlighted the potential antitumor effects of POMs. In 1974, Jasmin *et al.* found the inhibitory effect of $(NH_4)_{17}Na[NaSb_9W_{21}O_{86}]$ against sarcoma virus-induced tumors, paving the way for the antitumor applications of POMs.[16] As antimony (Sb) compounds have been medicinally used in cancer treatment for over a century, Sb-containing POMs have received increasing attention as antitumor agents. For example, $\{Co_4Sb_9W_{24}\}$,[17] $\{Na_{0.7}M_{5.3}Sb_2W_{18}\}$ (M = Ni/Co),[18] and $\{SbW_8O_{30}\}$[19] have all been reported to exert antitumor effects in various malignancies such as breast, lung, ovarian, and pancreatic cancers. Moreover, our recent work reported a water-soluble Sb-rich POM $\{Sb_{21}Tb_7W_{56}\}$ (POM-1), the Sb-rich POM with the highest number of Sb atoms.[20] POM-1 exhibited excellent antitumor activities *in vitro* and *in vivo*, in which the cytotoxicity of Sb-rich POM-1 was 18-fold higher than that of mono-Sb-containing $\{B-\alpha-SbW_9O_{33}\}$ precursor, suggesting the essential role of the architecture of POM also contributes to the antitumor activity.[20] However, POMs' antitumor effects appear to vary largely depending on the cell types. Despite these promising findings, the specific antitumor effects and mechanism of action, particularly against NSCLC cells, remain unknown warranting further investigation.

Herein, to further elucidate the antitumor potential of Sb-rich POM against NSCLC, POM-1 was employed to study the antitumor effects and mechanism in NSCLC cells. Specifically, we extensively assessed the efficacy of POM-1 in inhibiting the proliferation, migration, and invasion of NSCLC cells *in vitro* and *in vivo*. Moreover, we conducted comprehensive investigations into the molecular mechanisms underlying the antitumor activities of POM-1. This study provides a novel and integrative insight into the anti-cancer mechanism of Sb-rich POMs, which is of great significance for the development of lung cancer drugs.

2 Experimental section

2.1 Materials and methods

All chemicals, unless specified, were purchased from TargetMol (Shanghai, P. R. China). All compounds used for biological evaluations were of >95% purity. Human NSCLC cell lines A549 and H1299 were obtained from ATCC (American Type Culture Collection) and maintained in Roswell Park Memorial Institute 1640 Medium (RPMI 1640, Gibco, USA) supplemented with 10% (v/v) fetal bovine serum (Gibco, USA), 1% (v/v) penicillin and streptomycin (100 µg mL^{-1}, Invitrogen) in a humidified incubator containing 5% CO_2 at 37 °C. Male nude mice (6–8 weeks old, 18–22 g) were purchased from SLAC Laboratory Animal Co. Ltd (Shanghai, China). All animal experiments were approved by the Animal Ethics Committee of the College of Biological Science and Engineering, Fuzhou University (2019-SG-006) and carried out in strict accordance with the guidelines.

2.2 Preparation of POM-1

The precursor of $Na_9[B-\alpha-SbW_9O_{33}]\cdot19.5H_2O$ was synthesized based on the literature method and proved by Fourier transform infrared (FT-IR) spectroscopy.[21] POM-1 was synthesized and characterized in a manner similar to that of the literature previously reported by us.[20] Briefly, $Na_9[B-\alpha-SbW_9O_{33}]\cdot19.5H_2O$ (0.17 mmol, 0.480 g), $Tb(NO_3)_3\cdot6H_2O$ (0.27 mmol, 0.120 g), H_3BO_3 (0.82 mmol, 0.050 g), 3 mL H_2O and 5 mL *N,N*-dimethylformamide were added to a 25 mL Teflon-lined stainless steel autoclave with stirring for 10 min, and then the pH was adjusted to 6.0 by adding 200 µL of formic acid. After being stirred for 50 min, the solution was kept at 140 °C for three days, followed by cooling the solution at room temperature yielded yellow bar crystals of POM-1. The obtained POM-1 was examined by single crystal X-ray diffraction, as well as characterized by powder X-ray diffraction and FT-IR spectrometry, and the results agreed with the reported ones (Fig. S1 and S2†). In subsequent biological evaluations, POM-1 was diluted from a 1 mM stock in 10 mM phosphate buffer supplemented with 150 mM saline (PBS) using PBS or cell culture medium for *in vitro* experiments or 0.9% saline in animal models.

2.3 Cytotoxicity

Approximately 5000 cells, specifically A549 or H1299 cell lines, were dispensed into individual wells of 96-well cell culture plates containing 100 µL of 1640 medium per well. These plates were then placed within a controlled humidified incubator with a 5% CO_2 atmosphere at 37 °C. Upon achieving adherence, the cells were subjected to varying concentrations of compound POM-1 over specified durations as outlined. Subsequently, 10 µL Cell Counting Kit-8 (CCK-8) reagent (Dojindo, Japan) was meticulously introduced into each well, followed by an incubation period of precisely 2 hours within the aforementioned incubator settings, the absorbance of the contents within the wells was quantified using a microplate reader (Bio-Tek, Winooski, VT, USA) set at a wavelength of 450 nm.

2.4 Wound healing assay

Cells (H1299 or A549) were seeded in a 12-well plate at a density of 5×10^5 cells per well. After observing that the cells were completely confluent in about 24 hours, the confluent monolayer was scraped with a 10 µL pipette tip of the same specification and washed with PBS three times to remove floating cells. Then the cells were incubated with corresponding drugs and images of cells migrating into the scratch were captured at different time points (0 h and 24 h) by microscopy (Olympus, Japan), and the proportion of scratches at different time points was analyzed by Image J software to calculate the rate of cell migration.

2.5 Transwell invasion assay

For the invasion experiment, a 50-fold dilution of 100 µL BD Matrigel, with a concentration ranging between 0.2–0.3 mg mL^{-1}, was applied onto the transwell chamber layer (Corning, USA). Subsequently, the chamber was incubated in a constant

temperature incubator at 37 °C for 2 hours. After drug treatment, the cells were digested with trypsin, and counted after resuspending. Following two rounds of PBS washing, 10^5 cells were seeded into the upper layer of the transwell chamber in 200 μL serum-free 1640 medium. 600 μL of 1640 with 10% FBS was added into the lower layer of the transwell chamber. The cells were then incubated in a cell incubator (37 °C, 5% CO_2) for 24 hours. Subsequently, the remaining cells on the upper side of the membrane were removed using a cotton swab. The invaded cells were fixed with 4% paraformaldehyde (Beyotime, China) for 15 min, cleaned with PBS, and dyed with 0.1% crystal violet (Beyotime, China) for an additional 15 min, which was followed by the imaging of the invaded cells with a microscope (Olympus, Japan). Finally, the crystal violet was eluted with 33% acetic acid/water (V/V), and the invasion rates were calculated by measuring the absorbance at 570 nm using a microplate reader.

2.6 Annexin V-FITC-based apoptosis detection

The apoptosis assay was measured by Annexin V-FITC Apoptosis Detection Kit (Beyotime, China). For flow cytometry analysis, cells were digested with EDTA-free trypsin and collected. Then cells with resuspended with PBS containing 5 μL of Annexin V-FITC and 10 μL of PE. After incubation for 20 minutes in the dark, the cells were detected by flow cytometry with the channels of FL1 and FL2 (BD Biosciences, USA). For immunofluorescence analysis, cells were fixed with 4% paraformaldehyde and incubated with 200 μL binding buffer containing 5 μL Annexin V-FITC. Then the cells were measured under a fluorescence microscope (Olympus, Japan).

2.7 Western blot

Cells were washed and harvested in PBS after being treated with drugs. The pelleted cells were then suspended in the RIPA lysis buffer (Beyotime, China) with cocktail protease inhibitors. After centrifuging, the protein was extracted, and the protein concentration was measured by Enhanced BCA Protein Assay Kit (Beyotime, China). Afterward, the proteins were boiled with Sodium Dodecyl Sulfate (SDS) loading buffer under 100 °C for 5 minutes. Equal amounts of proteins were separated on the 12.5% SDS-PAGE (Polyacrylamide Gel Electrophoresis). Proteins on the gels were transferred onto a nitrocellulose membrane, blocked with 5% non-fat milk for 2 hours, and incubated with primary antibody at 4 °C overnight. After washing with Tris-buffer with saline and tween 20 (TBS-T, Beyotime, China) three times/10 minutes, the membranes were incubated with the corresponding secondary antibody at 4 °C for 2 h. After washing as before, protein bands were detected using a chemiluminescent detection system (Bio-rad, USA). The antibody against the cleaved caspase 3 was purchased from Cell Signaling Technology (CST9661S). The antibody against actin was purchased from Proteintech (23660-1-AP).

2.8 Colony formation assay

After H1299/A549 cells were treated with POM-1 for 24 hours, 1000 cells were seeded into the 6-well plate after digestion and PBS washing. Then, the cells were cultured under normal conditions for 10 days, fixed with 4% paraformaldehyde, stained with crystal violet, and photographed for observation. The proportion of clone formation was analyzed by Image J software to calculate the rate of cell proliferation.

2.9 Determination of intracellular lipid peroxidation

C11-BODIPY 581/591 (MedChemExpress, HY-D1301) was used as a lipid peroxidation sensor for the investigation of ferroptosis. H1299 cells (1×10^5) were individually seeded in six-well culture plates and incubated overnight at 37 °C with 5% CO_2. Once the cells adhered to the wells, they were treated with various concentrations of POM-1. After 24 hours of incubation, the cells were exposed to 5 μM of C11-BODIPY (boron-dipyrromethene) 581/591, which was diluted in a serum-free medium. Following a 30 minutes incubation period, the cells were washed thrice with PBS and subjected to imaging using a fluorescence microscope (Nikon SMZ18, Japan). Additionally, the fluorescence was quantitatively determined using the FL1 channel of a flow cytometer (BD Accuri C6 plus, America) after the cells were harvested through trypsin digestion.

2.10 A549-based lung cancer mouse model

A549 cells at a volume of 200 μL and a density of 2×10^7 cells per mL suspended in PBS with Matrigel were injected subcutaneously into the back of nude mice. After the tumors were visible, the mice were divided into 3 groups using a stratified random sampling method, control group, low dose POM-1 group (25 mg kg^{-1}, 1.3625 μmol kg^{-1}), and high dose POM-1 group (50 mg kg^{-1}, 2.7250 μmol kg^{-1}). The mice were administered with POM-1 once every second day according to the indicated experimental group, a total of nine doses were administered, and the changes in mice weight and tumor volume were recorded. The tumor volumes were calculated using the modified ellipsoid formula $1/2 \times (\text{length} \times \text{width}^2)$. The tumor tissues were resected and weighed after the mice were anesthetized by an inhalational administration with isopentane and sacrificed on day 17. Tumor tissues were also analyzed by (Hematoxylin and Eosin) H&E and Ki-67 staining. The assessment of tumor cell morphology in xenograft sections was performed according to the operation instructions.

2.11 Transcriptome analysis using RNA-seq

2.11.1 RNA extraction and library construction. Total RNA was isolated using a TRIzol total RNA extraction kit (TIANGEN, Cat. No. DP424), which yielded >2 μg of total RNA per sample. RNA quality was examined by 0.8% agarose gel electrophoresis and spectrophotometry. High-quality RNA with a 260/280 absorbance ratio of 1.8–2.2 was used for library construction and sequencing. Illumina library construction was performed according to the manufacturer's instructions (Illumina, USA). Oligo-dT primers are used to transverse mRNA to obtain cDNA (APExBIO, Cat. No. K1159). Amplify cDNA for the synthesis of the second chain of cDNA. Purify cDNA products by AMPure XP system (Beckman Coulter, Beverly, USA). After library construction, library fragments were enriched by PCR amplification and selected according to a fragment size of 350–550 bp. The library was quality-assessed using an Agilent 2100 Bioanalyzer (Agilent, USA). The library was sequenced using the

Illumina NovaSeq 6000 sequencing platform (Paired end150) to generate raw reads.

2.11.2 RNA-seq data analysis. Raw paired-end FASTQ reads were filtered by TrimGaloreto discard the adapters and low-quality bases *via* calling the Cutadapt tool. The clean reads obtained were then aligned to the hg19 human genome using HISAT2, followed by reference genome-guided transcriptome assembly and gene expression quantification using StringTie. Differentially expressed genes (DEGs) were identified by DEseq2 with a cut-off value of log 2|fold-change| > 1 and *p*-adjust < 0.05. The cluster Profiler was used to perform functional enrichment analysis for the annotated significant DEGs, the potential genes in identified modules based on gene ontology (GO) and Kyoto Encyclopedia of Genes and Genomes (KEGG) pathway categories. Terms with *P* value < 0.05 were considered significant. Gene set enrichment analysis (GSEA) was performed by the function in package cluster Profiler with a gene list sorted by log 2 fold-change.

2.12 Statistical analysis

Data are presented as the mean ± standard deviation (SD), all experiments were performed at least three times. The statistical significance was analyzed using two-way analysis of variance (ANOVA) followed by Bartlett's test using the GraphPad Prism 7 software. A *P* value of less than 0.05 was considered statistically significant.

3 Results

3.1 Structure and physicochemical properties of POM-1

POM-1 represents the rare example of a soluble and water-stable giant POM, which contains the largest number of Sb centers (21) yet found in POM chemistry. POM-1 can be viewed as a hexameric antimonotungstate encapsulating a 5p–4f $\{Sb^{III}_{13}$-$Sb^{V}_2Tb_7O_{63}(OH)_3(DMF)(H_2O)_6\}$ heterometallic cluster with the nanoscale sizes of *ca.* $2.6 \times 2.0 \times 1.9$ nm^3 (Fig. 1). POM-1 possess uniform dispersibility, good stability and biocompatibility in aqueous solutions, which have been investigated by electrospray ionization mass spectrometry and dynamic light scattering analysis in our previous report,[20] which has been confirmed to be critical for their biological functions.[22] Thus, POM-1 provides a unique case for treating NSCLC and investigating its intrinsic mechanisms.

3.2 Anti-proliferative and anti-invasive effects of POM-1 in NSCLC cells *in vitro*

To investigate the antitumor effect of POM-1 *in vitro*, cell proliferation of two NSCLC cell lines H1299 and A549 treated
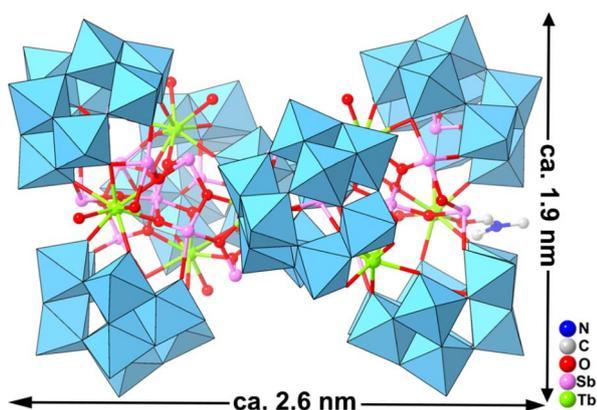

Fig. 1 Polyhedral and ball-stick representation of POM-1. Polyhedral key: WO$_6$, blue.
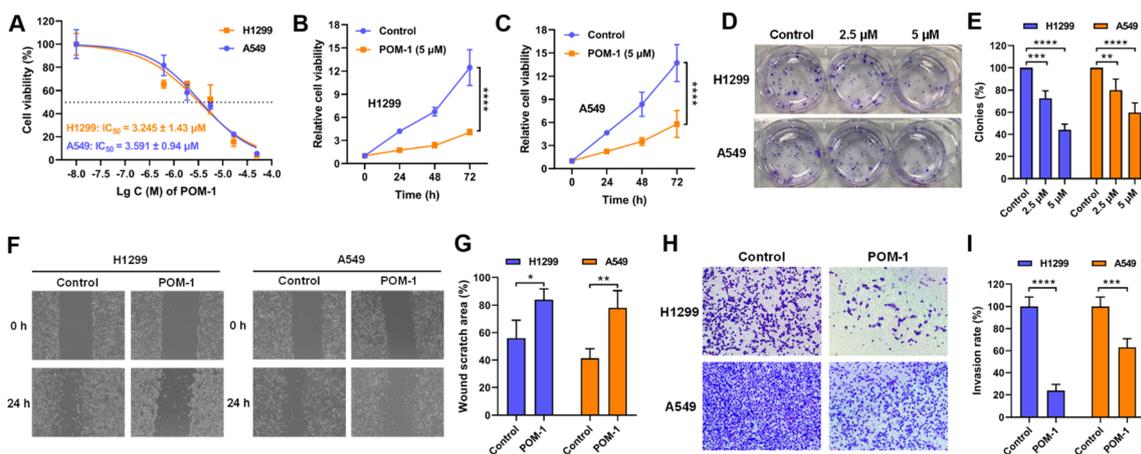

Fig. 2 POM-1 inhibited proliferation, migration and invasion of NSCLC cells *in vitro*. (A) Dose-dependent cytotoxicity of POM-1 against H1299 and A549 cells. (B) Time-dependent cytotoxicity of POM-1 against H1299 and (C) A549 cells. Cell viability was evaluated by CCK-8 assay. (D) Colony formation of H1299 and A549 cells with treatment with 2.5 μM or 5 μM POM-1 for 24 hours. Colonies were visualized by crystal violet staining. (E) Quantitation of colony formation rates in D. (F) Representative images of H1299 and A549 cells treated with 5 μM POM-1 in wound healing assay at 0 hours and 24 hours. (G) The proportion of wound scratch area at 24 h was analyzed and calculated with the software of Image J by setting the area at 0 h as 100%. (H) Representative images of H1299 and A549 cells treated with 5 μM POM-1 for 24 hours in transwell invasion assay. (I) The invasion rate of cells treated with POM-1 was calculated by determining A570 nm in crystal violet stained cells. The values are represented as mean ± SD (*n* = 3). *P < 0.05, **P < 0.01, ***P < 0.001, and ****P < 0.0001.

with POM-1 (0–50 μM) were first assessed. After a 72 h treatment, the half maximal inhibitory concentration (IC_{50}) of POM-1 against H1299 and A549 were 3.245 and 3.591 μM, respectively (Fig. 2A). Similarly, by treating with 5 μM POM-1 for 72 h, the proliferation of H1299 and A549 cells was sharply inhibited by 8.41 ($P < 0.0001$) and 7.93 ($P < 0.0001$) folds, respectively (Fig. 2B and C). Furthermore, the result of the clonogenic assay demonstrated that the colony formation of H1299 and A549 cells was inhibited by 56% ($P < 0.0001$) and 40.33% ($P < 0.0001$), respectively, indicating the severely impaired reproductivity of NSCLC cells (Fig. 2D and E). Additionally, the anti-migratory and anti-invasive effects of POM-1 were evaluated using the wound healing assay and Transwell invasion assay, respectively, *in vitro*. Treatment with 5 μM POM-1, led to reductions in the migration rates of H1299 and A549 cells by 28.05% ($P = 0.0212$) and 36.88% ($P = 0.0049$), respectively (Fig. 2F and G), as well as inhibiting invasion rates by 76.18% ($P < 0.0001$) and 36.98% ($P < 0.001$), respectively (Fig. 2H and I). Collectively, these findings imply the potent efficacy of POM-1 in suppressing the

proliferation, migration, and invasion of lung cancer cell lines *in vitro*. Interestingly, although exhibiting comparable anti-proliferative and anti-migratory efficacies in both H1299 and A549 cell lines, POM-1 demonstrated higher efficiency in inhibiting the invasion of H1299. This result may be attributed to the KRAS mutation in A549 cells which contributed to higher invasiveness.[23] In contrast, H1299 does not contain this mutation. In addition to our present study, the higher invasiveness of A549 cells compared to H1299 cells has also been observed in other studies.[24,25] Therefore, due to the higher invasiveness of A549, POM-1 exhibited lower efficiency in suppressing A549's invasion compared to suppressing H1299's invasion.

3.3 POM-1 suppressed tumor growth *in vivo*

Subsequently, we evaluated the anti-tumor effects of POM-1 against NSCLC *in vivo* by transplanting A549 cells in nude mice. Tumor-bearing mice were randomly divided into three groups ($N = 6$–7) and administrated daily with saline supplemented with 0, 25, or 50 mg kg^{-1} POM-1 for 17 days. Tumor
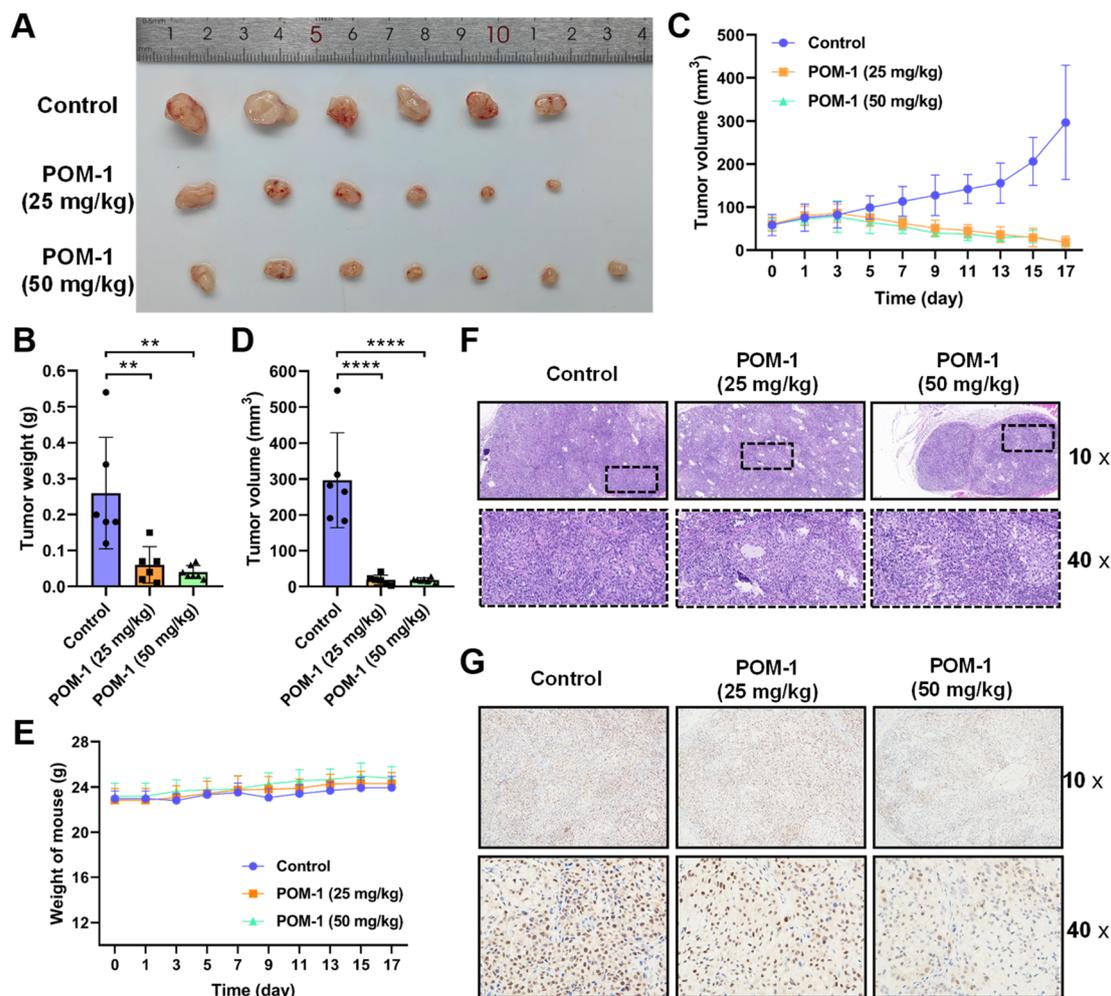

Fig. 3 POM-1 suppressed tumor growth in an NSCLC xenograft mouse model. (A) Photographs of tumor tissues resected from the mice on day 17 days after the daily treatment with saline (control), 25 mg kg^{-1}, or 50 mg kg^{-1} POM-1. (B) Tumor weights in panel A. (C) Tumor volumes determined every second day in tumor-bearing mice in the above groups. (D) Tumor volumes on day 17. (E) Body weights were determined every second day in tumor-bearing mice treated with saline or POM-1. (F) Representative images of histopathological sections of tumor tissue with H&E staining and (G) Ki-67 staining. The values are represented as mean ± SD ($n = 6$–7). **$P < 0.01$ and ****$P < 0.0001$.

volumes and body weights were monitored daily throughout the experiment, with tumor tissues being resected and weighed upon the mice's sacrifice on day 17. Over the entire observation period, at both low-dose (25 mg kg^{-1}) and high-dose (50 mg kg^{-1}), POM-1 exhibited remarkable efficacies in the suppression of tumor growth (Fig. 3A–D), while showing a minimal impact on the body weights of the treated mice (Fig. 3E). According to the weights of resected tumor tissues, low and high doses of POM-1 suppressed tumor growth by 76.92% ($P = 0.0046$) and 84.62% ($P = 0.0015$), respectively (Fig. 3B). Furthermore, histopathological examination with hematoxylin–eosin (HE) staining demonstrated large area of apoptosis and necrosis in tumor tissues, with no apparent toxic effects observed in the liver and spleen (Fig. 3F & S3†). Additionally, immunohistochemical staining with anti-Ki67 antibody revealed that the Ki-67 expression was remarkably decreased in POM-1-treated groups (Fig. 3G), indicating the lower aggressiveness of tumor growth. Therefore, these results underscore the pronounced antitumor activity and biosafety of POM-1 *in vivo*.

3.4 Transcriptomic analysis

After confirming POM-1's antineoplastic activities *in vitro* and *in vivo*, we further endeavored to elucidate its mechanism of action by conducting transcriptomic analysis on H1299 cells treated with or without POM-1. KEGG enrichment analysis of differentially expressed genes (DEGs) indicated notable variations primarily in genes associated with ferroptosis and TGF-β signaling pathway (Fig. 4A). Similarly, gene set enrichment analysis (GSEA) also demonstrated enrichment of DEG signatures related to ferroptosis in H1299 cells treated with POM-1
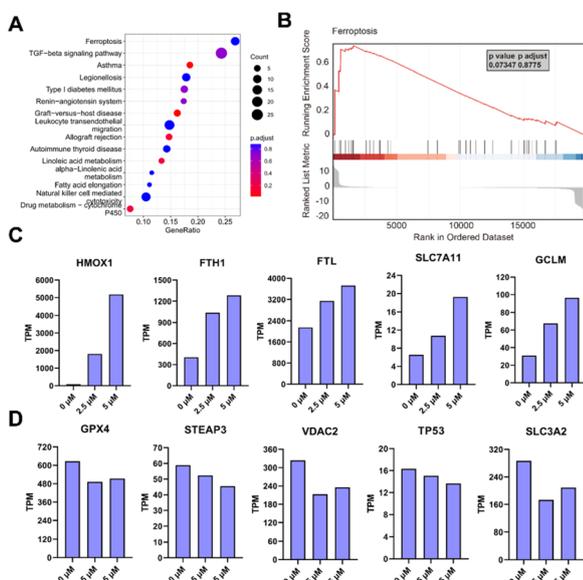

Fig. 4 Transcriptomic analysis on H1299 cells treated with saline or 5 μM POM-1. (A) GSEA enrichment of all genes and Top15 enriched pathways. (B) Normalized enrichment score (NES) of ferroptosis using GSEA analysis. (C) Up-regulated and (D) down-regulated DEGs of ferroptosis from POM-1 treated cells.

(Fig. 4B). Specifically, treatment with POM-1 led to the upregulation of mRNA expression levels of genes in Erastin-induced ferroptosis, including SLC7A11, GCLM, HMOX1, FTH1, and FTL (Fig. 4C & S4A†). Consistently, the downregulation of GPX4, STEAP3, and VDAC2 were also observed (Fig. 4D & S4B†). Considering the pivotal role of transforming growth factor-beta (TGF-β) signaling pathway in the initiation of apoptosis, these results suggested that POM-1 might induce a dual antitumor mechanism by synergistically inducing ferroptosis and apoptosis.

3.5 POM-1 induced ferroptosis in NSCLC cells

The ferroptotic effects instigated by POM-1 were subsequently validated *via* following experimental methodologies. First, we evaluated the potential reversal of the cytotoxicity of POM-1 in the presence of ferrostatin-1 (Fer-1), an identified ferroptosis inhibitor, with RSL3, an inhibitor of glutathione peroxidase 4 (GPX4), as a positive control (Fig. 5A, B & S5†). Based on IC$_{50}$ values, Fer-1 mitigated the cytotoxicity of POM-1 and RSL3 against H1299 by 5.8-fold and 5.4-fold, respectively. Additionally, in POM-1 treated cells, consistent with mRNA expression levels (Fig. 4C and D), the protein expression levels of HMOX1 and FTH1 demonstrated a dose-dependent augmentation, while the GPX4 level showed a dose-dependent reduction (Fig. 5C). Furthermore, the formation of lipid peroxides (LPO) was qualitatively visualized *via* fluorescence microscopy using C11-BODIPY 581/591 as a fluorescent probe, which can be oxidized by intracellular LPO causing a shift in the maximum emission peak from 590 (red) to 510 nm (green). As displayed in Fig. 5D & S6,† POM-1-treated H1299 cells exhibited diminished red fluorescence and enhanced green fluorescence, indicating that POM-1 dose-dependently elevated the intracellular LPO level. This observation was further corroborated through the quantitative assessment of intracellular LPO by flow cytometry, which demonstrated that by treating with 1 μM, 2.5 μM, and 5 μM POM-1, cytoplasmic LPO in H1299 was enhanced by 1.965 ($P = 0.1401$), 3.204 ($P = 0.0022$), and 5.659 ($P < 0.0001$) folds, respectively (Fig. 5E, F & S7†). Therefore, the aforementioned experimental evidences collectively elucidate the induction of ferroptosis by POM-1 in NSCLC cells.

3.6 POM-1 induced apoptosis of lung cancer cells

In accordance with findings from the transcriptomic analysis, alterations in genes associated with the TGF-β signaling pathway were observed, suggesting a potential induction of apoptosis in POM-1-treated cells. We thus investigated the involvement of apoptosis in the antitumor mechanism of POM-1. Firstly, pericellular expression of phosphatidylserine was visualized by Annexin V-FITC under a fluorescence microscope, revealing a dose-dependent elevation in Annexin V$^+$ cells in both H1299 and A549 cells upon POM-1 treatment (Fig. 6A). Consistently, the early apoptotic and necrotic cells were quantitatively determined by flow cytometry employing Annexin V/PI staining. After the treatment of 5 μM POM-1, the percentages of early apoptotic cells (Annexin V$^+$/PI$^-$) were significantly increased by 7.29% and 11.61% in H1299 and A549 cells, respectively, while the percentages of late apoptotic cells
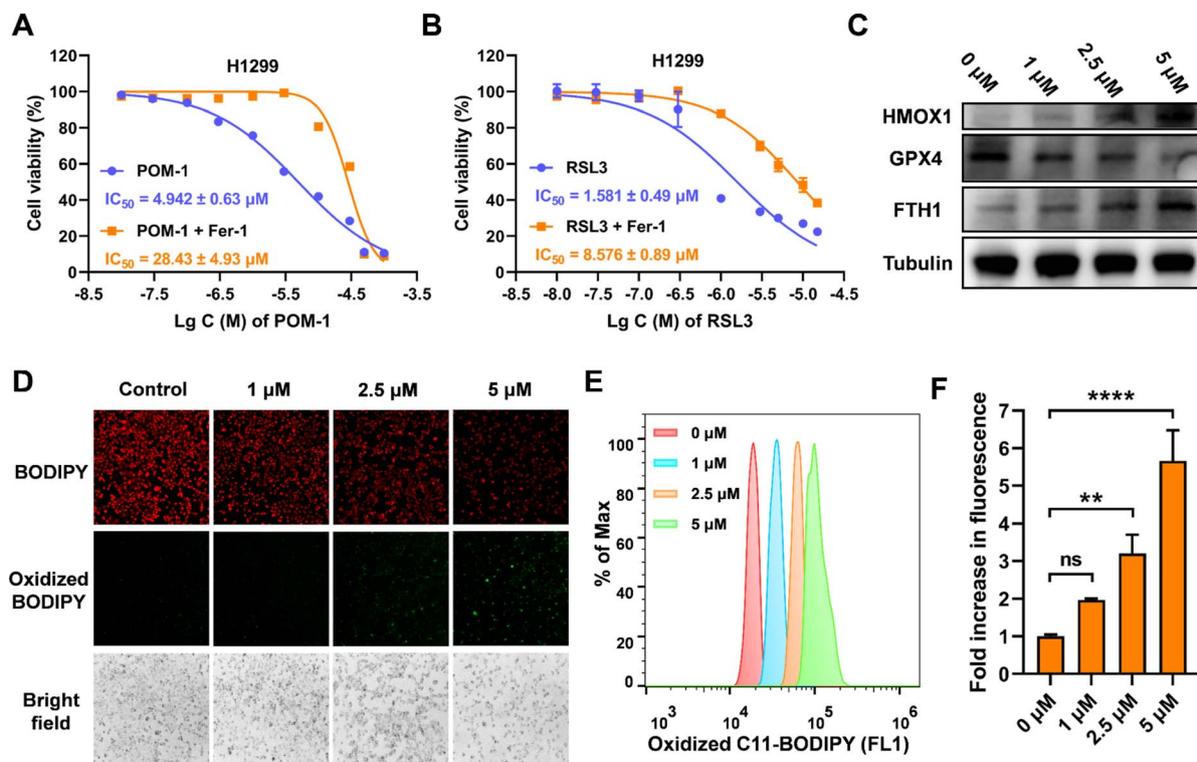
Fig. 5 Ferroptosis induced by POM-1 in H1299 cells. (A and B) Dose-dependent cytotoxicity of POM-1 (A) and RSL3 (B) against H1299 cells in the presence or absence of ferrostatin-1 (Fer-1). (C) Protein expression of HMOX1, GPX4, and FTH1 identified by immunoblot. (D) Fluorescence microscopy imaging of LPO induced by POM-1 visualized by C11-BODIPY 581/591 in H1299 cells. (E and F) C11-BODIPY 581/591 oxidized probe was quantitatively analyzed using a flow cytometer after treatment with different concentrations of POM-1. The values are represented as mean $\pm$ SD ($n = 3$). **$P < 0.01$ and ****$P < 0.0001$.
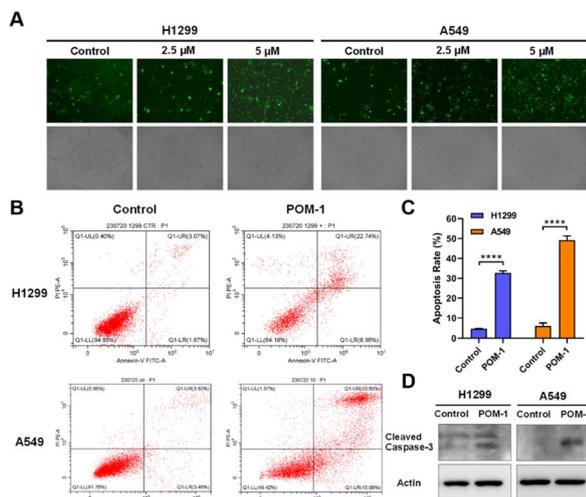

Fig. 6 Apoptosis induced by POM-1 in NSCLC cells. (A) Fluorescence imaging of phosphatidylserine by FITC-Annexin V in H1299 and A549 cells treated with POM-1. (B) Flow cytometry-based Annexin V/PI apoptosis analysis in H1299 and A549 cells treated with 5 μM POM-1. (C) Quantitation of apoptosis rates in panel B. (D) Expression of cleaved caspase-3 in H1299 and A549 cells treated with 5 μM POM-1 determined by western blot. The values are represented as mean $\pm$ SD ($n = 3$). ****$P < 0.0001$.

(Annexin V$^+$/PI$^+$) were increased by 19.67% ($P < 0.0001$) and 30.1% ($P < 0.0001$), respectively (Fig. 6B and C). In addition, the elevated protein expression of cleaved caspase 3, a hallmark of apoptosis, also demonstrated an obvious increase in apoptotic H1299 and A549 cells treated with 5 μM POM-1 (Fig. 6D). Collectively, the above results substantiate the apoptosis mechanism, which significantly contributes to the cytotoxicity of POM-1 in NSCLC cancer cells.

4 Discussion

Sb complexes with various organic ligands have been used for anticancer therapy, notably in acute promyelocytic leukemia.[26] These organic ligands have been confirmed to be essential for their antitumor effects.[27] Both Sb(v) and Sb(iii) compounds exhibit antitumor activities, however, the priority of their effectiveness is still controversial.[28,29] POMs offer versatile frameworks for incorporating Sb atoms and functional organic ligands, particularly those with a high number of Sb atoms, making Sb-containing POMs of considerable interest as antitumor agents. Typically, similar to other antitumor metal complexes, e.g. platinum drugs, the primary antitumor mechanism of Sb-based drugs is also by inducing apoptosis.[30] Not surprisingly, most reported Sb-containing POMs, as well as other metal POMs, have been confirmed to exert antitumor

effects by triggering apoptotic pathways.[17,18,31] For instance, Liu *et al.* reported that a giant heterometallic POM activated the p53 signaling pathway to induce apoptosis in cervical cancer cells.[32] Besides, a Cu(II)-containing POM induced apoptosis in hepatoma, marked by elevated levels of matrix metalloproteinases.[33] Our group and others have verified that the disruption of mitochondrial functions leading to apoptosis can also be attributed to the antitumor mechanism of POMs.[34,35] Apart from apoptosis, the only known regulated cell death (RCD) involved in POM-induced cell death is pyroptosis, a type of RCD associated with intrinsic inflammation.[36,37] Jia *et al.* discovered that a Bi-containing POM, $\{BiW_8O_{30}\}$, was capable of inducing pyroptosis in both tumor and endothelial cells.[38]

We previously synthesized a Sb-rich POM with the highest number of Sb, $\{Sb_{21}Tb_7W_{56}\}$, designated as POM-1 in this study. POM-1 initiated the p53 signaling pathway inducing apoptosis of breast cancer cells.[34] In our current study, we discovered mRNA levels of genes relevant to ferroptosis have been regulated by POM-1 by conducting transcriptomic analysis. Through multidimensional validations, we demonstrated the upregulation of ferroptosis-associated proteins and intracellular LPO accumulations, solidly indicating ferroptosis inside NSCLC cells. This study, for the first time, reveals ferroptosis as a new antitumor mechanism of POMs. Additionally, consistent with our previous study, POM-1 also triggered apoptosis in NSCLC cells, resulting in a complex mechanism synergizing ferroptosis and apoptosis. Together with our previously reported evidences, the antitumor mechanism of POM-1 against NSCLC is elucidated in Scheme 1. First, POM-1 penetrates cells and disrupts the mitochondrial membrane. Mitochondrial dysfunction subsequently activates the p53 signaling pathway,[39] leading to the activation of caspases and externalization of phosphatidylserine,[40] which signs the apoptosis of tumor cells. On the other hand, POM-1 increases the expression of HMOX1, enhancing heme degradation and resulting in iron accumulation in tumor cells.[41] Simultaneously, GPX4 is downregulated leading to the reduction of GSH level thereby protecting the generated LPO.[42] Additionally, FTH1 expression was increased

in response to the elevated intracellular iron concentrations.[43] The above intricate molecular mechanisms culminate in the substantial generation of LPO, ultimately causing the disruption of membrane integrity and cell death.[44] In summary, the synergism of apoptosis and ferroptosis guarantees the high antitumor effects of POM-1, which also reveals a new insight into the mechanisms underlying POM-induced cancer therapy.

The synergism of apoptosis and ferroptosis in cancer therapy is an emerging concept that leverages the distinct mechanisms of these two forms of cell death to enhance the efficacy of cancer treatments. The rationale for synergizing apoptosis and ferroptosis is grounded in the idea that by hitting cancer cells from multiple angles, the chances of effectively killing them and preventing recurrence are significantly increased. By simultaneously targeting both pathways, it raises the following advantages: (1) overcoming resistance mechanisms: many cancers, including H1299 used in our current study, develop resistance to apoptosis through mutations in key regulatory genes (*e.g.*, p53, Bcl-2) or overexpression of anti-apoptotic proteins.[45] These cells might still be vulnerable to ferroptosis. Conversely, cancer cells resistant to ferroptosis due to high antioxidant capacity or altered iron metabolism may remain susceptible to apoptosis-inducing agents.[46] (2) Complementary mechanisms: apoptosis and ferroptosis operate through different biochemical and molecular pathways. Apoptosis is caspase-dependent and involves DNA fragmentation and cell shrinkage, while ferroptosis is iron-dependent and characterized by lipid peroxidation and membranal dysfunction. Targeting both pathways can provide a more comprehensive attack on cancer cells. (3) Enhancing antitumor efficacy: simultaneous activation of apoptosis and ferroptosis can increase the overall cell death rate, ensuring that a higher proportion of cancer cells are eradicated. In some cases, the combination of apoptosis and ferroptosis-inducing agents can lead to synthetic lethality, where the combined effect of targeting both pathways is greater than the sum of their individual effects. (4) Reducing side effects: using a combination of agents to induce both apoptosis and ferroptosis can allow for lower doses of each drug, potentially reducing the side effects associated with high-dose single-agent therapies.

In contrast to polyoxotungstate used in our current study, polyoxovanadates have been more extensively studied for their biological functions.[47] This is largely due to polyoxovanadates' similarity to phosphates in chemical structure, making them effective inhibitors of kinases and phosphatases.[48] Structural insights into the molecular interactions between kinases/phosphates and polyoxovanadates have also been elucidated by X-ray crystallography.[49] However, it is important to note that in many crystal structures, polyoxovanadates formed during the long-term soaking with vanadate ions (VO_4^{3-}). Given their broad-spectrum inhibitory activity against kinases and phosphatases, polyoxovanadates are also considered to possess significant interests as anticancer agents.[47] Their anticancer mechanisms include those relevant to such enzyme inhibition, *e.g.* intervention with cell cycle, ion transportation, mRNA synthesis, ATP consumption, and mechanisms irrelevant to enzyme inhibition, including membrane attack, morphological
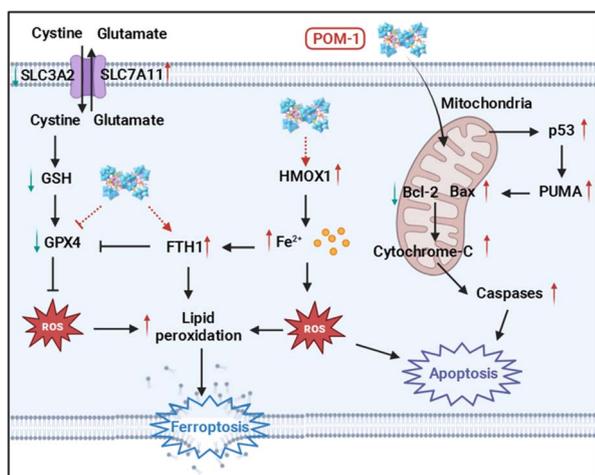
Scheme 1 Illustration of the antitumor mechanism of POM-1.

changes, oxidative stress.[14] Interestingly, similar to our polyoxotungstate POM-1, a polyoxovanadate has also been confirmed to target mitochondria and inducing apoptosis.[50] Furthermore, oxidative stress and LPO formation was also observed in cells treated with polyoxovanadates,[15,51] while additional experimental validations, *e.g.* protein expression, mRNA levels, and ferroptosis inhibitors, are required to fully confirm the mechanism of ferroptosis by polyoxovanadates.

5   Conclusions

Our study demonstrates compelling evidence that Sb-rich POM-1 effectively impeded the proliferation, migration, and invasion of NSCLC cells *in vitro*, as well as exerted significant antitumor efficacy in a xenograft NSCLC mouse model. Transcriptomic analysis revealed alterations in mRNA levels within ferroptosis- and apoptosis-related signaling pathways. Furthermore, we employed ferroptosis inhibitors, immunoblotting, subcellular LPO imaging, and flow cytometric quantitation of LPO to validate ferroptosis induced by POM-1. Concurrently, the pro-apoptotic effects of POM-1 were confirmed using confocal PS staining, Annexin V/PI flow cytometric analysis, and immunoblotting for Caspase-3 activation. In summary, our findings not only suggest Sb-rich POM-1 as an effective agent for the suppression of NSCLC proliferation and metastasis, but also provide novel and integrative insights into the anti-cancer mechanism of POMs. Notably, for the first time, this research identifies ferroptosis as an antitumor mechanism of POMs. This study presents both theoretical and practical significance for the future development of safer and more effective POM-based antitumor agents.

Data availability

Crystallographic data for POM-1 has been deposited at the The Cambridge Crystallographic Data Centre (CCDC) under 2124838 and can be obtained from **https://www.ccdc.cam.ac.uk/structures/**. The datasets supporting this article have been uploaded as part of the ESI.†

Author contributions

Hui-Ping Xiao synthesized the polyoxometalate. Jie-Wei Lin, Lei-Lei, Wu, and Peng-Cheng Li, Yang Zhou performed the antitumor experiments. Ming-Dong Huang contributed to sample preparation and assisted with project implement. Yang Zhou, Zhi-Xin Li and Hui-Ping Xiao wrote the paper with guidance from all corresponding authors. Zhi-Xin Li, Dong Xie, Peng Xu, Xin-Xiong Li conceived the study, supervised the experiments, and contributed to the writing and revision of the manuscript.

Conflicts of interest

There are no conflicts to declare.

Acknowledgements

Notes and references

1 S. Chen, M. Li, T. Weng, D. Wang and J. Geng, *J. Mater. Chem. B*, 2023, **11**, 5715–5747.

2 H. Yin, J. Ma, L. Chen, S. Piao, Y. Zhang, S. Zhang, H. Ma, Y. Li, Y. Qu, X. Wang and Q. Xu, *Cell. Physiol. Biochem.*, 2018, **46**, 471–481.

3 A. A. Thai, B. J. Solomon, L. V. Sequist, J. F. Gainor and R. S. Heist, *Lancet*, 2021, **398**, 535–554.

4 H. Zhu, H. Liu, J. H. Zhu, S. Y. Wang, S. S. Zhou, M. Kong, Q. Mao, F. Long, Z. J. Fang and S. L. Li, *Food Funct.*, 2021, **12**, 2225–2241.

5 C. M. Granadeiro, D. Julião, S. O. Ribeiro, L. Cunha-Silva and S. S. Balula, *Coord. Chem. Rev.*, 2023, **476**, 214914.

6 Q.-s. Lai, X.-X. Li and S.-T. Zheng, *Coord. Chem. Rev.*, 2023, **482**, 215077.

7 J.-C. Liu, J.-W. Zhao, C. Streb and Y.-F. Song, *Coord. Chem. Rev.*, 2022, **471**, 214734.

8 A. Ebrahimi, L. Krivosudský, A. Cherevan and D. Eder, *Coord. Chem. Rev.*, 2024, **508**, 215764.

9 H. Hu, L. Lian, X. Ji, W.-L. Zhao, H. Li, W. Chen, H. N. Miras and Y.-F. Song, *Coord. Chem. Rev.*, 2024, **503**, 215640.

10 K. Xia, K. Yamaguchi and K. Suzuki, *Angew. Chem., Int. Ed.*, 2022, **62**, e202214506.

11 A. V. Anyushin, A. Kondinski and T. N. Parac-Vogt, *Chem. Soc. Rev.*, 2020, **49**, 382–432.

12 M. B. Colovic, M. Lackovic, J. Lalatovic, A. S. Mougharbel, U. Kortz and D. Z. Krstic, *Curr. Med. Chem.*, 2020, **27**, 362–379.

13 A. Bijelic, M. Aureliano and A. Rompel, *Chem. Commun.*, 2018, **54**, 1153–1169.

14 M. Aureliano, N. I. Gumerova, G. Sciortino, E. Garribba, A. Rompel and D. C. Crans, *Coord. Chem. Rev.*, 2021, **447**, 214143.

15 A. Bijelic, M. Aureliano and A. Rompel, *Angew. Chem., Int. Ed.*, 2019, **58**, 2980–2999.

16 C. Jasmin, J.-C. Chermann, G. Herve, A. Teze, P. Souchay, C. Boy-Loustau, N. Raybaud, F. Sinoussi and M. Raynaud, *JNCI, J. Natl. Cancer Inst.*, 1974, **53**, 469–474.

17 Z. M. Zhang, X. Duan, S. Yao, Z. Wang, Z. Lin, Y. G. Li, L. S. Long, E. B. Wang and W. Lin, *Chem. Sci.*, 2016, 7, 4220–4229.

18 H. Zhao, L. Tao, F. Zhang, Y. Zhang, Y. Liu, H. Xu, G. Diao and L. Ni, *Chem. Commun.*, 2019, **55**, 1096–1099.

19 L. Gong, W. Ding, Y. Chen, K. Yu, C. Guo and B. Zhou, *Angew. Chem., Int. Ed.*, 2021, **60**, 8344–8351.

20 H. P. Xiao, Y. S. Hao, X. X. Li, P. Xu, M. D. Huang and S. T. Zheng, *Angew. Chem., Int. Ed.*, 2022, **61**, e202210019.

21 M. Bösing, I. Loose, H. Pohlmann and B. Krebs, *Chem.–Eur. J.*, 1997, **3**, 1232–1237.

22 N. I. Gumerova and A. Rompel, *Chem. Soc. Rev.*, 2020, **49**, 7568–7601.

23 G. Rao, M. Pierobon, I. K. Kim, W. H. Hsu, J. Deng, Y. W. Moon, E. F. Petricoin, Y. W. Zhang, Y. Wang and G. Giaccone, *Sci. Rep.*, 2017, **7**, 7066.

24 T. Sun, C. Song, G. Zhao, S. Feng, J. Wei, L. Zhang, X. Liu, Z. Li and H. Zhang, *Cell Death Dis.*, 2023, **14**, 814.

25 Y. Li, P. Zhang, G. Tang, J. Zhong, Z. Wang and B. Zhu, *Sci. Rep.*, 2024, **14**, 17069.

26 P. Sharma, D. Perez, A. Cabrera, N. Rosas and J. L. Arias, *Acta Pharmacol. Sin.*, 2008, **29**, 881–890.

27 Y. Cheng and Y. Qi, *Adv. Anticancer Agents Med. Chem.*, 2017, **17**, 1046–1069.

28 S. K. Hadjikakou, I. I. Ozturk, C. N. Banti, N. Kourkoumelis and N. Hadjiliadis, *J. Inorg. Biochem.*, 2015, **153**, 293–305.

29 C. Liu, J. Shin, S. Son, Y. Choe, N. Farokhzad, Z. Tang, Y. Xiao, N. Kong, T. Xie, J. S. Kim and W. Tao, *Chem. Soc. Rev.*, 2021, **50**, 2260–2279.

30 B. Desoize, *Anticancer Res.*, 2004, **24**, 1529–1544.

31 F. Lu, M. Wang, N. Li and B. Tang, *Chemistry*, 2021, **27**, 6422–6434.

32 J. C. Liu, J. F. Wang, Q. Han, P. Shangguan, L. L. Liu, L. J. Chen, J. W. Zhao, C. Streb and Y. F. Song, *Angew. Chem., Int. Ed.*, 2021, **60**, 11153–11157.

33 Z. Zhou, D. Zhang, L. Yang, P. Ma, Y. Si, U. Kortz, J. Niu and J. Wang, *Chem. Commun.*, 2013, **49**, 5189–5191.

34 H. P. Xiao, Y. S. Hao, X. X. Li, P. Xu, M. D. Huang and S. T. Zheng, *Angew. Chem., Int. Ed.*, 2022, **61**, e202210019.

35 L. Gong, W. Ding, Y. Chen, K. Yu, C. Guo and B. Zhou, *Angew. Chem., Int. Ed.*, 2021, **60**, 8344–8351.

36 P. Yu, X. Zhang, N. Liu, L. Tang, C. Peng and X. Chen, *Signal Transduction Targeted Ther.*, 2021, **6**, 128.

37 X. Wei, F. Xie, X. Zhou, Y. Wu, H. Yan, T. Liu, J. Huang, F. Wang, F. Zhou and L. Zhang, *Cell. Mol. Immunol.*, 2022, **19**, 971–992.

38 D. Jia, L. Gong, Y. Li, S. Cao, W. Zhao, L. Hao, S. Li, B. Pang, C. Zhang, S. Li, W. Zhang, T. Chen, L. Dong, B. Zhou and D. Yang, *Angew. Chem., Int. Ed.*, 2021, **60**, 21449–21456.

39 A. J. Levine, *Nat. Rev. Cancer*, 2020, **20**, 471–480.

40 L. Galluzzi, O. Kepp and G. Kroemer, *Oncogene*, 2012, **31**, 2805–2808.

41 B. Hassannia, P. Vandenabeele and T. Vanden Berghe, *Cancer Cell*, 2019, **35**, 830–849.

42 W. Zhang, Y. Liu, Y. Liao, C. Zhu and Z. Zou, *Biomed. Pharmacother.*, 2024, **174**, 116512.

43 Y. Fang, X. Chen, Q. Tan, H. Zhou, J. Xu and Q. Gu, *ACS Cent. Sci.*, 2021, **7**, 980–989.

44 X. Jiang, B. R. Stockwell and M. Conrad, *Nat. Rev. Mol. Cell Biol.*, 2021, **22**, 266–282.

45 A. Lopez, D. E. Reyna, N. Gitego, F. Kopp, H. Zhou, M. A. Miranda-Roman, L. U. Nordstrom, S. R. Narayanagari, P. Chi, E. Vilar, A. Tsirigos and E. Gavathiotis, *Nat. Commun.*, 2022, **13**, 1199.

46 X. Chen, J. Li, R. Kang, D. J. Klionsky and D. Tang, *Autophagy*, 2021, **17**, 2054–2081.

47 F. Carvalho and M. Aureliano, *Int. J. Mol. Sci.*, 2023, **24**, 5043.

48 E. J. Baran, *Coord. Chem. Rev.*, 2024, **502**, 215549.

49 M. Aureliano, N. I. Gumerova, G. Sciortino, E. Garribba, C. C. McLauchlan, A. Rompel and D. C. Crans, *Coord. Chem. Rev.*, 2022, **454**, 214344.

50 S. S. Soares, C. Gutierrez-Merino and M. Aureliano, *Aquat. Toxicol.*, 2007, **83**, 1–9.

51 M. Aureliano, A. L. De Sousa-Coelho, C. C. Dolan, D. A. Roess and D. C. Crans, *Int. J. Mol. Sci.*, 2023, **24**, 5382.